

Highly Luminescent Lanthanide Complexes of 1-Hydroxy-2-pyridinones

Evan G. Moore, Jide Xu, Christoph J. Jocher, Ingrid Castro-Rodriguez, and Kenneth N. Raymond*

Department of Chemistry, University of California, Berkeley, California 94720-1460

Received November 1, 2007

The synthesis, X-ray structure, stability, and photophysical properties of several trivalent lanthanide complexes formed from two differing bis-bidentate ligands incorporating either alkyl or alkyl ether linkages and featuring the 1-hydroxy-2-pyridinone (1,2-HOPO) chelate group in complex with Eu(III), Sm(III), and Gd(III) are reported. The Eu(III) complexes are among some of the best examples, pairing highly efficient emission ($\Phi_{\text{tot}}^{\text{Eu}} \sim 21.5\%$) with high stability ($pK_{\text{a}} \sim 18.6$) in aqueous solution, and are excellent candidates for use in biological assays. A comparison of the observed behavior of the complexes with differing backbone linkages shows remarkable similarities, both in stability and photophysical properties. Low temperature photophysical measurements for a Gd(III) complex were also used to gain insight into the electronic structure and were found to agree with corresponding time-dependent density functional theory (TD-DFT) calculations for a model complex. A comparison of the high resolution Eu(III) emission spectra in solution and from single crystals also revealed a more symmetric coordination geometry about the metal ion in solution due to dynamic rotation of the observed solid state structure.

Introduction

The ability to detect analytes such as DNA,¹ proteins,² or other biologically active molecules³ at small concentrations and in the presence of a complicated matrix or even *in vivo* remains a challenging task. Many of these bioassays often rely on lanthanide fluorescence, which can furnish detection limits in the nano and picomolar region.⁴ Specifically, their sharp “atom-like” emission spectra, large Stokes shift, and long-lived luminescence makes trivalent lanthanide cations such as Eu(III) very attractive reporters for these assays. Using both spectral and temporal discrimination of the luminescent signal from background autofluorescence enables highly sensitive assays,^{5,6} such as the dissociation enhanced lanthanide fluoro immuno assay (DELFLIA) techniques first commercialized by Wallace, which use a polyaminocarboxylate chelate of Eu(III).⁷ However, the DELFLIA format is heterogeneous and suffers from the limitation that the

fluorescent signal cannot be traced until the end of the assay, when the non-fluorescent Ln(III) chelate is converted to a highly fluorescent form by the addition of a sensitizing β -diketonate enhancement solution. Hence, the preparation of efficient lanthanide sensitizers which also form very stable complexes in dilute aqueous solution is an active area of research, since they can be utilized directly and/or covalently bound to a particular biomolecule for use in less expensive and less time-consuming homogeneous assay formats.

Some earlier examples of systems utilized in this manner and which have been very successful were based on Eu(III) cryptates originally developed by Lehn.⁸ However, in these cases, optimum results often required the addition of an augmenting agent such as anionic fluoride to displace residual inner sphere water molecules, which otherwise strongly quench Eu(III) centered luminescence.⁹ More recently, several relatively stable Ln(III) complexes with a tetrapodal ligand design incorporating four picolinate chelating moieties have been prepared, which were found to be quite efficient sensitizers of Tb(III), with overall luminescence quantum yield of $\Phi_{\text{tot}}^{\text{Tb}} = 45\%$ and, to a lesser extent, for Eu(III) ($\Phi_{\text{tot}}^{\text{Eu}} = 7.0\%$).¹⁰ Conditional stability constant (pM) measurements¹¹ showed that these water soluble complexes possessed

* To whom correspondence should be addressed. Phone: +1 510 642 7219. Fax: +1 510 486 5283. E-mail: raymond@socrates.berkeley.edu.

- (1) Vitzthum, F.; Bernhagen, J. *Rec. Res. Dev. Anal. Biochem.* **2002**, *2*, 65–93.
- (2) Leca-Bouvier, B.; Blum, L. *J. Anal. Lett.* **2005**, *38*, 1491–1517.
- (3) Kimura, H.; Matsumoto, K.; Mukaida, M. *J. Anal. Toxicol.* **2005**, *29*, 799–805.
- (4) Jones, S. G.; Lee, D. Y.; Wright, J. F.; Jones, C. N.; Tear, M. L.; Gregory, S. J.; Burns, D. D. *J. Fluoresc.* **2001**, *11*, 13–21.
- (5) Handl, H. L.; Gillies, R. J. *Life Sci.* **2005**, *77*, 361–371.
- (6) Petoud, S.; Cohen, S. M.; Bünzli, J.-C. G.; Raymond, K. N. *J. Am. Chem. Soc.* **2003**, *125*, 13324–13325.

- (7) Hemmila, I.; Dakubu, S.; Mikkala, V. M.; Siitari, H.; Lovgren, T. *Anal. Biochem.* **1984**, *137*, 335–43.
- (8) Alpha, B.; Balzani, V.; Lehn, J. M.; Perathoner, S.; Sabbatini, N. *Angew. Chem.* **1987**, *99*, 1310–11.
- (9) Mathis, G. *Clin. Chem.* **1993**, *39*, 1953–9.

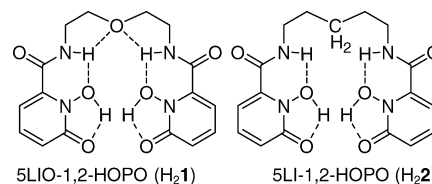
solution stability that exceeds that of EDTA ($pEu = 15.5$). However, the observed excitation maximum was quite high in energy, with a λ_{max} at 274 nm. For biological applications, it is preferable that such complexes allow for sensitization of the metal using the lowest possible energy (longer wavelength) in order to minimize autofluorescence and to increase the penetration depth of excitation into the sample.¹²

Another recently described Eu(III) chelate, which has the advantage of red-shifted excitation at 335 nm, was reported by Matsumoto et al.¹³ This compound is a polycarboxylate derivative of a terpyridine complex and, according to preliminary stability assessment by competition with EDTA, is several orders of magnitude more stable than the [Eu(EDTA)] complex at pH 8. However, the synthesis of the complex is quite lengthy and the intensity of the resulting Eu(III) emission remains only moderate, with $\Phi_{tot}^{Eu} = 9.1\%$.

Another approach pioneered by Parker has been the covalent attachment of a variety of sensitizing chromophores to the macrocyclic DO3A platform, most recently utilizing azaxanthenes and azathioxanthenes as the light absorbing chromophore which has extended the absorption envelope as far as ca. 380 nm.¹⁴ While stability data were not reported, these DO3A macrocyclic based complexes are known to form stable and very kinetically inert complexes with Ln(III) cations,¹⁵ and they almost certainly possess sufficient stability for biological applications. Despite their long wavelength absorbance, these chromophores have a relatively small energy gap between their first excited singlet and the lowest energy sensitizing triplet state, which facilitated their use as sensitizer for both Tb(III) and Eu(III). However, their luminescence performance is limited by incomplete energy transfer to the metal (as evidenced by residual ligand centered emission) and, more importantly, the presence of a single water molecule in the first coordination sphere ($q = 1$). Nonetheless, the observed quantum yields with Eu(III) were still very good with $\Phi_{tot}^{Eu} = 8.9\%$, and for Tb(III), improved values as high as $\Phi_{tot}^{Tb} = 24\%$ were reported, remarkably high for a $q = 1$ complex.

The sensitization of trivalent lanthanides with the simple 1-hydroxy-2-pyridinone (1,2-HOPO) chromophore has been previously reported,^{16,17} specifically focusing on the $[ML_3(H_2O)_2]$ or $[ML_4]^-$ complexes with Tb(III), Dy(III), and Eu(III), which were also characterized by X-ray crystallography. In those studies, the focus was on Tb(III), which

Chart 1. Tetradentate 1,2-HOPO Based Ligands for Sensitization of Eu(III) and Sm(III)



displayed an impressive quantum yield of $\Phi_{tot}^{Tb} = 20\%$ in methanol solution, whereas the performance of the Eu(III) complex was much less striking with $\Phi_{tot}^{Eu} = 0.3\%$. Recently, we discovered that the 6-amide derivatives of 1,2-HOPO have vastly improved performance for Eu(III), and we have reported on their excellent sensitization efficiency.¹⁸ The tetradentate ligand, 5LIO-1,2-HOPO (H_21 , Chart 1), is remarkable in that its ML_2 complex with Eu(III) combines both a very high quantum yield ($\Phi_{tot}^{Eu} = 21.5\%$) with exceptionally good aqueous stability ($pEu = 18.6$). Indeed, a comparison of the stability data for Fe(III), Al(III), and Ga(III) complexes of 1,2-HOPO's indicates that this group acts as a very strong chelator for Lewis acidic trivalent ions such as Ln(III),^{19,20} while conversely forming significantly weaker complexes with divalent ions such as Cu(II) or Zn(II).²¹ Furthermore, another important advantage of using the 6-carboxy-1-hydroxy-2-pyridinone precursor is the facile preparation of multidentate 1,2-HOPO based ligands which are able to exploit the chelate effect for higher complex stabilities.²² These ligands also allow a certain measure of control over the Ln(III) coordination sphere, by providing steric bulk and helping prevent the coordination of inner sphere solvent molecules, when compared to the bidentate analogues. In this paper, we elaborate on our previous communication¹⁸ to include the alkyl linked ligand 5LI-1,2-HOPO (H_22 , Chart 1) in complex with Eu(III), and as a result of the now completed photophysical characterization of the chromophore, we broaden the scope to include the complexes of both ligands with Sm(III).

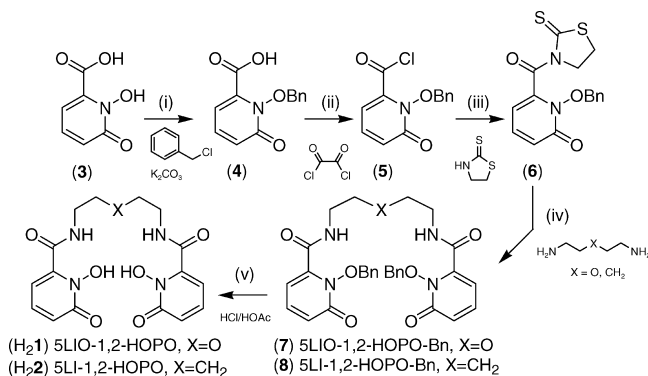
Experimental Section

General. All solvents for reactions were dried using standard methodologies. Thin-layer chromatography (TLC) was performed using precoated Kieselgel 60 F254 plates. Flash chromatography was performed using EM Science Silica Gel 60 (230–400 mesh). NMR spectra were obtained using either Bruker AM-300 or DRX-500 spectrometers operating at 300 (75) MHz and 500 (125) MHz for 1H (or ^{13}C), respectively. 1H (or ^{13}C) chemical shifts are reported in ppm relative to the solvent resonances, taken as δ 7.26 (δ 77.0) and δ 2.49 (δ 39.5), respectively, for $CDCl_3$ and $(CD_3)_2SO$ while coupling constants (J) are reported in Hz. The following standard abbreviations are used for characterization of 1H NMR signals: s = singlet, d = doublet, t = triplet, q = quartet, quin = quintet, m

- (10) Chatterton, N.; Bretonniere, Y.; Pecaut, J.; Mazzanti, M. *Angew. Chem., Int. Ed.* **2005**, *44*, 7595–7598.
 (11) $pM = -\log_{10}[M]_{free}$. It is defined as the negative log of the free metal (M) concentration under pH 7.4 conditions with $10 \mu M [L]_{total}$ and $1 \mu M [M]_{total}$.
 (12) Weissleder, R.; Ntziachristos, V. *Nat. Med.* **2003**, *9*, 123–8.
 (13) Nishioka, T.; Yuan, J.; Yamamoto, Y.; Sumitomo, K.; Wang, Z.; Hashino, K.; Hosoya, C.; Ikawa, K.; Wang, G.; Matsumoto, K. *Inorg. Chem.* **2006**, *45*, 4088–4096.
 (14) Atkinson, P.; Findlay, K. S.; Kielar, F.; Pal, R.; Parker, D.; Poole, R. A.; Puschmann, H.; Richardson, S. L.; Stenson, P. A.; Thompson, A. L.; Yu, J. *Org. Biomol. Chem.* **2006**, *4*, 1707–1722.
 (15) Kumar, K.; Chang, C. A.; Francesconi, L. C.; Dischino, D. D.; Malley, M. F.; Gougoutas, J. Z.; Tweedle, M. F. *Inorg. Chem.* **1994**, *33*, 3567–75.
 (16) Tedeschi, C.; Azema, J.; Gornitzka, H.; Tisnes, P.; Picard, C. *Dalton Trans.* **2003**, 1738–1745.
 (17) Tedeschi, C.; Picard, C.; Azema, J.; Donnadiou, B.; Tisnes, P. *New J. Chem.* **2000**, *24*, 735–737.

- (18) Moore, E. G.; Xu, J.; Jocher, C. J.; Werner, E. J.; Raymond, K. N. *J. Am. Chem. Soc.* **2006**, *128*, 10648–10649.
 (19) Clarke, E. T.; Martell, A. E.; Reibenspies, J. *Inorg. Chim. Acta* **1992**, *196*, 177–83.
 (20) Li, Y. J.; Martell, A. E. *Inorg. Chim. Acta* **1993**, *214*, 103–11.
 (21) Farkas, E.; Kozman, E.; Petho, M.; Herlihy, K. M.; Micera, G. *Polyhedron* **1998**, *17*, 3331–3342.
 (22) Moore, E. G.; Jocher, C. J.; Xu, J.; Werner, E. J.; Raymond, K. N. *Inorg. Chem.* **2007**, *46*, 5468–5470.

Scheme 1. Synthesis of 5LIO-1,2-HOPO (H₂1) and 5LI-1,2-HOPO (H₂2) via the Readily Accessible 1,2-HOPO-Bn-thiaz (6)



= multiplet, dd = doublet of doublets. Fast-atom bombardment mass spectra (FABMS) were performed using 3-nitrobenzyl alcohol (NBA) or thioglycerol/glycerol (TG/G) as the matrix. Elemental analyses were performed by the Microanalytical Laboratory, University of California, Berkeley, CA.

Synthesis. Detailed synthesis of several relevant precursors (see Scheme 1) including the thiazolidine activated derivative 1,2-HOPO-Bn-thiaz (6) starting from commercially available 6-bromo-picolinic acid have been described elsewhere.²³ Similarly, the synthesis of 5LIO-1,2-HOPO (H₂1) and its Eu(III) complex as the pyridinium salt, C₅H₆N[Eu(1)₂], have been previously reported.¹⁸ A detailed synthesis of 5LI-1,2-HOPO (H₂2) and its Eu(III) complex, C₅H₆N[Eu(2)₂], is described below, and corresponding complexes of Sm(III) and Gd(III) were prepared using the same procedure.

5LI-1,2-HOPO-Bn (8). To a solution of 1,2-HOPO-Bn-thiaz (6) (1.22 g, 3.52 mmol) in dry CH₂Cl₂ (30 mL) was added neat 1,5-pentanediamine (184 mg, 1.8 mmol). The resulting mixture was left to stir overnight, and ensuing purification of the reaction mixture was realized by removal of the solvent at reduced pressure and subsequent loading of the residue onto a flash silica column. Gradient elution with 2–6% MeOH in CH₂Cl₂ allowed separation of the benzyl-protected precursor, 5LI-1,2-HOPO-Bn, as a pale yellow oil (0.9 g, 92%). ¹H NMR (300 MHz, CDCl₃): δ 1.18 (quin, 2H), 1.39 (quin, 4H), 3.17 (q, 4H), 5.26 (s, 4H), 6.32 (dd, 2H), 6.62 (dd, 2H), 6.78 (t, 2H), 7.26–7.45 (m, 12H). ¹³C NMR (75 MHz, CDCl₃): δ 23.4, 27.9, 39.3, 79.1, 105.9, 123.2, 128.4, 129.2, 129.9, 133.2, 138.5, 142.9, 158.5, 160.3.

5LI-1,2-HOPO (H₂2). 5LI-1,2-HOPO-Bn (8) (557 mg, 1.0 mmol) was dissolved in a conc. HCl/glacial AcOH mixture (20 mL, 1:1 (v/v)), and was stirred at room temperature for 2 days. Filtration followed by removal of the solvent yielded a beige residue, which was washed with Et₂O to give 5LI-1,2-HOPO as a beige powder (344 mg, 74%). ¹H NMR (300 MHz, (CD₃)₂SO): δ 1.35 (quin, 2H), 1.46 (quin, 4H), 3.18 (q, 4H), 6.26 (dd, 2H), 6.55 (dd, 2H), 7.37 (dd, 2H), 8.73 (t, 2H). MS (FAB+): 377 (MH⁺). Elemental analysis for C₁₇H₂₀N₄O₆·2HCl·H₂O (*M*_r = 467.30 g·mol⁻¹), Calcd. (Found): C, 43.69 (43.75); H, 5.17 (4.93); N, 11.98 (11.65).

C₅H₆N[Eu(5LI-1,2-HOPO)₂] (C₅H₆N[Eu(2)₂]). A solution of EuCl₃·6H₂O (37 mg, 0.1 mmol) in MeOH (1 mL) was added to a stirred solution of H₂2 (94 mg, 0.20 mmol) in MeOH (5 mL). The clear solution became turbid after 2 drops of dry pyridine were added. The mixture was heated to reflux for 6 h under nitrogen, during which time the complex deposited as a white precipitate. This solid was isolated by filtration, rinsed with cold MeOH, and

dried to give the pyridinium salt of the complex (80 mg, 82%) as a white solid. Elemental analysis for EuC₃₄H₃₆N₈O₁₂·C₅H₆N (*M*_r = 980.77 g·mol⁻¹). Calcd. (Found): C, 47.76 (47.45); H, 4.32 (4.22); N, 12.85 (12.67). MS (ES⁻): 900.1 (M⁻). Crystals of the complex suitable for X-ray diffraction studies were prepared by vapor diffusion of ether into a wet methanol solution of the complex in the presence of excess dimethylamine.

Physical Methods

Crystallography. Crystals suitable for X-ray analysis were mounted on a Kapton loop using Paratone N hydrocarbon oil and measured at low temperature using a Siemens SMART CCD²⁴ area detector with graphite monochromated Mo Kα radiation. Cell constants and orientation matrices were obtained from least-squares refinement. The resulting data were integrated by the program SAINT²⁵ and corrected for Lorentz and polarization effects. Data were also analyzed for agreement and possible absorption using XPREP.²⁶ An empirical absorption correction based on the comparison of redundant and equivalent reflections was applied using SADABS.²⁷ Equivalent reflections where appropriate were merged, and no decay correction was applied. The structures were solved within the WinGX²⁸ package by direct methods using SIR92²⁹ and expanded using a full-matrix least-squares techniques with SHELXL-97.³⁰ Hydrogen atoms were positioned geometrically, with C–H = 0.93 Å for CH aromatic, C–H = 0.97 Å for CH₂ methylene, N–H = 0.89 Å, and C–H = 0.96 Å for CH₃ methyl. Hydrogen atoms were constrained to ride on their parent atoms, with *U*_{iso}(H) values set at 1.2*U*_{eq}(C) for all H atoms. Resulting drawings of molecules were produced with ORTEP-3.³¹

Solution Thermodynamics. Experimental protocols and details of the apparatus closely followed those of a previous study for related ligands.³² The 5LI-1,2-HOPO (H₂2) ligand and corresponding [Eu(2)₂]⁻ complex protonation constants were examined by potentiometric titrations (pH vs total proton concentration) using Hyperquad.³³ Spectrophotometric titrations (absorbance vs pH) were examined using pHab³⁴ for data analysis. Both methods result in identical *pK*_a values within experimental error.

All experiments were performed at 25 °C and with 0.1 M

(24) SMART, version 5.059: Area-Detector Software Package; Bruker Analytical X-ray Systems, Inc.: Madison, WI, 1999.

(25) SAINT, version 7.07B: SAX Area-Detector Integration Program; Siemens Industrial Automation, Inc.: Madison, WI, 2005.

(26) XPREP, version 6.12: Part of the SHELXTL Crystal Structure Determination Package; Bruker AXS Inc.: Madison, WI, 1995.

(27) Sheldrick, G. SADABS, version 2.10: Siemens Area Detector Absorption Correction Program; University of Göttingen: Göttingen, Germany, 2005.

(28) WinGX 1.70.01 Farrugia, L. J. *J. Appl. Crystallogr.* **1999**, *32*, 837–838.

(29) SIR92 Altomare, A.; Cascarano, G.; Giacovazzo, C.; Guagliardi, A. *J. Appl. Crystallogr.* **1993**, *26*, 343–350.

(30) Sheldrick, G. M. SHELXL97, Programs for Crystal Structure Analysis; Institut für Anorganische Chemie der Universität: Göttingen, Germany, 1998.

(31) ORTEP-3 for Windows Farrugia, L. J. *J. Appl. Crystallogr.* **1997**, *30*, 565.

(32) Johnson, A. R.; O'Sullivan, B.; Raymond, K. N. *Inorg. Chem.* **2000**, *39*, 2652–2660.

(33) Gans, P.; Sabatini, A.; Vacca, A. *Talanta* **1996**, *43*, 1739–1753.

(34) Gans, P.; Sabatini, A.; Vacca, A. *Annal. Chim. (Rome)* **1999**, *89*, 45–49.

(23) Xu, J.; Churchill, D. G.; Botta, M.; Raymond, K. N. *Inorg. Chem.* **2004**, *43*, 5492–5494.

KCl as electrolyte. Each determination results from three independent experiments, where each experiment consists of two titrations, first against 0.1 M HCl followed by reverse titrations against 0.1 M KOH. Additionally, protonation constants of the metal complex at low pH values were measured, where each experiment consists of one titration from pH 3 to 1.6. A correction of the liquid–liquid junction potential was performed in the course of pH electrode calibration, as detailed elsewhere.³⁵ Equilibration times for titrations were 150 and 210 s for ligand only and metal complex titrations, respectively. Ligand and metal concentrations were in the range of 0.1–0.5 mM for potentiometric titrations. For spectrophotometric titrations, the ligand and metal complex concentrations were ca. 0.01 mM.

As a result of the strength of the binding interaction, and the highly acidic nature of the ligand, the Eu(III) ML₂ complex formation constants with either ligand could not be determined directly. As such, for the determination of the ML₂ formation constant, β_{120} , spectrophotometric titrations versus the known competitor, DTPA, were performed between pH 5 and 9 with the competitor concentration ranging from 0.01 μ M to 0.12 mM. Additional spectrophotometric titrations with differing concentrations of Eu(III) and ligand between pH 3 and 1.6 in the absence of the DTPA competitor then allowed the determination of the constants β_{121} and β_{110} from refinements with fixed β_{120} .

Photophysics. UV–visible absorption spectra were recorded on a Cary 300 double beam absorption spectrometer using quartz cells of 1.0 cm path length. Emission spectra were acquired on a HORIBA Jobin Yvon IBH FluoroLog-3 spectrofluorimeter. Spectra were reference corrected for both the excitation light source variation (lamp and grating) and the emission spectral response (detector and grating). Quantum yields were determined by the optically dilute method³⁶ using the following equation:

$$\frac{\Phi_x}{\Phi_r} = \left[\frac{A_r(\lambda_r)}{A_x(\lambda_x)} \right] \left[\frac{I(\lambda_r)}{I(\lambda_x)} \right] \left[\frac{\eta_x^2}{\eta_r^2} \right] \left[\frac{D_x}{D_r} \right]$$

where A is the absorbance at the excitation wavelength (λ), I is the intensity of the excitation light at the same wavelength, η is the refractive index, and D is the integrated luminescence intensity. The subscripts “x” and “r” refer to the sample and reference, respectively. Quinine sulfate in 1.0 N sulfuric acid was used as the reference ($\Phi_r = 0.546$).³⁶

Luminescence lifetimes were determined with a HORIBA Jobin Yvon IBH FluoroLog-3 spectrofluorimeter, adapted for time-resolved measurements. A sub-microsecond Xenon flash lamp (Jobin Yvon, 5000XeF) was used as the light source, coupled to a double grating excitation monochromator for spectral selection. The input pulse energy (100 nF discharge capacitance) was ca. 50 mJ, yielding an optical pulse duration of less than 300 ns at fwhm. A thermoelectrically cooled single photon detection module (HORIBA Jobin Yvon IBH, TBX-04-D) incorporating a fast risetime PMT, wide band-

width preamplifier, and picosecond constant fraction discriminator was used as the detector. Signals were acquired using an IBH DataStation Hub photon counting module, and data analysis was performed using the commercially available DAS 6 decay analysis software package from HORIBA Jobin Yvon IBH. Goodness of fit was assessed by minimizing the reduced chi squared function, χ^2 , and a visual inspection of the weighted residuals. Each trace contained at least 10 000 points, and the reported lifetime values result from at least three independent measurements.

Typical sample concentrations for absorption and fluorescence measurements were ca. 10^{-5} – 10^{-6} M, and 1.0 cm cells in quartz suprasil or equivalent were used. Solid state measurements performed for the Eu(III) complexes were accomplished by fixing a dispersion of crystalline material to a glass microscope slide with Crazy Glue cyanoacrylate based adhesive. The luminescence spectra and lifetimes in this case were measured using front-face excitation at 22.5°.

Computational Studies. Ground state density functional theory (DFT) and time-dependent DFT (TD-DFT) calculations were performed at the Molecular Graphics and Computational Facility, College of Chemistry, University of California, Berkeley. In both cases, the B3LYP/6-311G++(d,p) basis set provided in Gaussian’03 was used, with simplified input structures derived from a previously reported¹⁸ crystal structure. All calculations were done in the gas phase, and geometry optimizations were performed with no symmetry restraints.

Results and Discussion

Synthesis and Structure. The first reported synthesis of a 6-amide functionalized 1-hydroxy-2-pyridinone (1,2-HOPO) chelate group appeared more than 20 years ago,³⁷ wherein the 1-hydroxy-2-pyridinone-6-carboxylic acid (**3**, Scheme 1) was first activated with phosgene gas and, then, coupled with an amine backbone to provide an amide linked multidentate 1,2-HOPO ligand scaffold. However, this procedure is somewhat unattractive since phosgene is highly toxic and, moreover, the yields of these coupling reactions were quite low (ca. 15–30%). Additionally, the separation and purification of the final products are sometimes difficult, in most cases requiring purification by HPLC which limits the scale of the synthesis.

A more attractive approach toward the synthesis of 1,2-HOPO derivatives has since been developed,^{18,23} as illustrated in Scheme 1 for the 5LIO-1,2-HOPO (**H₂1**) and 5LI-1,2-HOPO (**H₂2**) ligands. This procedure relies on the inherently greater acidity of the *N*-hydroxyl group, when compared to the carboxylic acid, which allows for near quantitative and selective benzyl protection. Upon treatment with oxalyl chloride, the benzyl protected 1,2-HOPO acid (**4**) can be easily converted to a 1,2-HOPO acid chloride (**5**), which reacts with primary or secondary amines to afford amide linked benzyl protected products.

The intermediate 1,2-HOPO acid chloride (**5**) is a very

(35) Martell, A. E.; Smith, R. M., Ed. *Critical Stability Constants*; 1974; Vol. 1, pp 263–270.

(36) Crosby, G. A.; Demas, J. N. *J. Phys. Chem.* **1971**, *75*, 991–1024.

(37) White, D. L.; Durbin, P. W.; Jeung, N.; Raymond, K. N. *J. Med. Chem.* **1988**, *31*, 11–18.

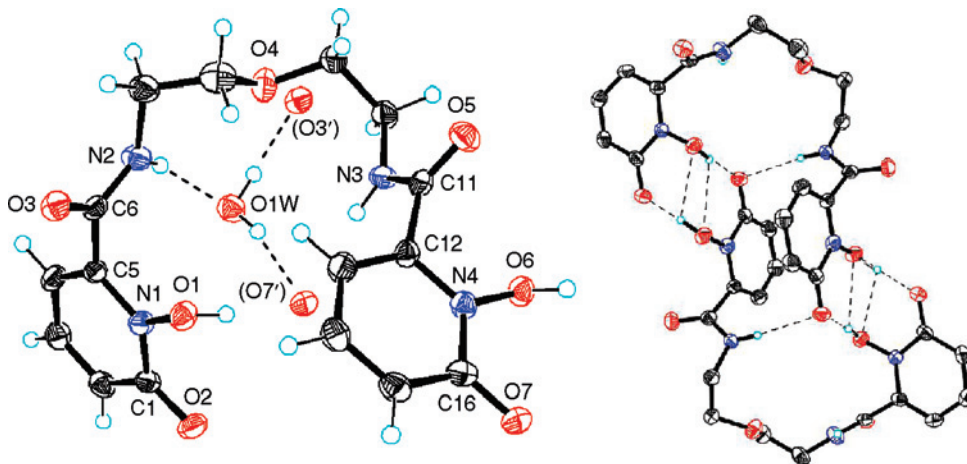


Figure 1. Two views of the crystal structure of (H_21) that illustrate the intermolecular hydrogen-bonding network (dashed lines—atoms labeled in parenthesis are symmetry related) and π stacking interactions which link each molecule into dimers in the unit cell packing. Selected H atoms have been omitted for clarity and non-H atoms are drawn at the 50% probability level.

reactive species and should be used immediately after preparation. Alternately, the benzyl protected 1,2-HOPO acid can also be activated toward subsequent amide bond formation by various reagents such as NHS, HOBT, or 2-mercaptothiazolidine using DCC as the coupling agent and DMAP as a catalyst. The activated NHS ester, HOBT ester, and thiazolidine readily react with a large variety of backbone amines to form the desired benzyl-protected 1,2-HOPO intermediates (**7**, **8**), which can be easily purified by flash chromatography on a preparative scale. As with the 1,2-HOPO acid chloride (**5**), the activated NHS and HOBT ester are not isolated in pure form, but rather generated and used in situ due to their reactivity. The 1,2-HOPO-Bn-thiaz (**6**) is therefore of particular interest since it can be easily separated and purified by flash chromatography and can also be stored since it is not sensitive to water and does not decompose. In most cases, the 1,2-HOPO-Bn-thiaz (**6**) selectively reacts with primary amines to afford the desired benzyl protected products in excellent yield and the loss of its characteristic yellow color can also be used as a visual indicator to determine the end point of the amide coupling reaction. The deprotection of the ligands proceeds smoothly under strongly acidic conditions to afford the desired products after removal of the solvent at reduced pressure in analytically pure form and in good yield.

X-ray quality crystals of H_21 were obtained via vapor diffusion of diethyl ether into a solution of the ligand in methanol. Two views of the resulting structure are shown in Figure 1, and crystal data is summarized in Table 1. Perhaps the most striking feature of this structure is the unusual geometry adopted by the ligand, likely a result of both intra- and intermolecular hydrogen bonding and also to a lesser extent π stacking between adjacent 1,2-HOPO rings (vide infra). Both of the individual 1,2-HOPO rings (defined by C_1-C_5 and N_1 , and $C_{12}-C_{16}$ and N_4) are planar, with very small root-mean-square (rms) values (0.0032 and 0.0168, respectively), and the adjacent amide groups (defined by C_6, O_3, N_2 and C_{11}, O_5, N_3) are similarly also planar. As

with similar structures reported previously,³⁸ these amide groups are not coplanar with the adjacent 1,2-HOPO ring system, instead lying almost orthogonal with dihedral angles of ca. 88.8° and 62.2° , respectively. The observed short C—O bond lengths between the C_1-O_2 and $C_{16}-O_7$ atoms at 1.26 and 1.27 Å, respectively, indicate that the ligand is predominately in the “keto” form. Indeed, 1,2-HOPO based ligand systems have previously been referred to as “cyclic hydroxamic acids” rather than as the tautomeric conjugated aromatic ring system, based on the similarity of UV–visible spectra to simpler analogs which cannot undergo this keto–enol tautomerisation.³⁹

An examination of the crystal packing for H_21 reveals a secondary arrangement of two distinct ligands to form dimers, which are held together by the π stacking of adjacent 1,2-HOPO ring systems at a separation of ca. 3.4 Å and a complex network of intra- and intermolecular hydrogen bonds. For example, the protons of the phenolic O1 and O6 atoms form complementary bifurcated intermolecular H-bonding interactions with the keto O7 ($O_1-H_1 \cdots O_7 = 1.75$ Å) and neighboring phenolic O6 atom ($O_1-H_1 \cdots O_6 = 2.46$ Å), and keto O2 ($O_6-H_6 \cdots O_2 = 1.57$ Å) and neighboring phenolic O1 atoms ($O_6-H_6 \cdots O_1 = 2.52$ Å), respectively. An additional intermolecular interaction between the amide N3 proton and keto O7 atom ($N_3-H_3 \cdots O_7 = 2.13$ Å) was also noted. Lastly, the presence of a single cocrystallized solvent-water molecule may also have had a significant influence on the observed ligand geometry, since this molecule makes a total of three intermolecular H-bonding contacts ($N_2-H_2A \cdots O_{1W} = 2.11$ Å, $O_{1W}-H_{1W1} \cdots O_3 = 1.91$ Å, and $O_{1W}-H_{1W2} \cdots O_7 = 2.12$ Å) which link adjacent dimer units.

The complexation of either the 5LIO-1,2-HOPO (H_21) or 5LI-1,2-HOPO (H_22) ligands with various $LnCl_3 \cdot 6H_2O$ salts

(38) Scarrow, R. C.; Riley, P. E.; Abu-Dari, K.; White, D. L.; Raymond, K. N. *Inorg. Chem.* **1985**, *24*, 954–967.

(39) Cunningham, K. G.; Newbold, G. T.; Spring, F. S.; Stark, J. *J. Chem. Soc.* **1949**, 2091–2094.

(40) Seitz, M.; Oliver, A. G.; Raymond, K. N. *J. Am. Chem. Soc.* **2007**, *129*, 11153–11160.

Table 1. Summary of Crystal Data Obtained for 5LJO-1,2-HOPO (H₂I) and 5LI-1,2-HOPO (H₂O) with Several Ln(III) Complexes

	H ₂ I·H ₂ O	C ₄ H ₁₂ N[Eu(D ₂)] ^a	C ₄ H ₁₂ N[Sm(D ₂)·CH ₃ OH·H ₂ O	C ₄ H ₁₂ N[Gd(D ₂)]	C ₂ H ₈ N[Eu(2I ₂)·(C ₃ H ₇ NO) ₂	C ₂ H ₈ N[Sm(2I ₂)·(C ₃ H ₇ NO) _{1.5}
empirical formula	C ₁₆ H ₂₀ N ₄ O ₈	C ₃₆ H ₄₄ N ₉ O ₁₄ Eu	C ₃₇ H ₅₀ N ₉ O ₁₆ Sm	C ₃₆ H ₄₄ N ₉ O ₁₄ Gd	C ₄₂ H ₅₇ N ₁₁ O ₁₄ Eu	C _{40.5} H _{54.5} N _{10.5} O _{13.5} Sm
mol. wt [g·mol ⁻¹]	396.36	978.76	1027.21	984.05	1091.95	1054.8
crystal system	monoclinic	monoclinic	monoclinic	monoclinic	monoclinic	monoclinic
space group	<i>P</i> ₂ / <i>1</i> / <i>n</i>	<i>P</i> ₂ / <i>1</i> / <i>n</i>	<i>P</i> ₂ / <i>1</i> / <i>c</i>	<i>P</i> ₂ / <i>1</i> / <i>c</i>	<i>P</i> ₂ / <i>1</i> / <i>n</i>	<i>P</i> ₂ / <i>1</i> / <i>n</i>
<i>a</i> [Å]	15.272 (13)	10.0579 (16)	8.6048 (5)	10.028 (5)	17.3141 (19)	17.3156 (18)
<i>b</i> [Å]	6.836 (6)	17.848 (3)	18.4988 (11)	17.771 (5)	13.1648 (14)	13.1786 (14)
<i>c</i> [Å]	17.852 (15)	22.642 (4)	26.6387 (16)	22.564 (5)	22.461 (2)	22.469 (2)
α [deg]	90	90	90	90	90	90
β [deg]	108.307 (11)	92.781 (2)	90.6180(5)	111.087 (19)	112.104 (1)	112.105 (1)
γ [deg]	90	90	90	90	90	90
volume [Å ³]	1769 (3)	4059.8 (12)	4240.1 (4)	3752.0 (2)	4743.4 (9)	4750.4(9)
<i>Z</i>	4	4	4	4	4	4
density, ρ [g·cm ⁻³]	1.488	1.601	1.609	1.742	1.529	1.475
absorption coefficient, μ [mm ⁻¹]	0.121	1.623	1.467	1.852	1.399	1.309
<i>F</i> (000)	832	1992	2100	1996	2244	2146
crystal size [mm ³]	0.18 × 0.14 × 0.03	0.40 × 0.20 × 0.07	0.30 × 0.20 × 0.02	0.18 × 0.14 × 0.02	0.18 × 0.12 × 0.12	0.15 × 0.14 × 0.09
temperature [°C]	-145 (2)	-138 (2)	-155 (2)	-145 (2)	-145 (2)	-149 (2)
wavelength	0.71073	0.71073	0.71073	0.71073	0.71073	0.71073
θ range for data collection [deg]	3.29–24.71	3.46–26.40	2.30–26.39	4.08–23.26	3.25–26.36	3.42–25.35
limiting indices	-17 < <i>h</i> < 15, -8 < <i>k</i> < 6, -20 < <i>l</i> < 20	-12 < <i>h</i> < 12, -22 < <i>k</i> < 12, -27 < <i>l</i> < 27	10 < <i>h</i> < 10, -21 < <i>k</i> < 21, -33 < <i>l</i> < 30	-11 < <i>h</i> < 11, -19 < <i>k</i> < 16, -25 < <i>l</i> < 19	-21 < <i>h</i> < 15, -16 < <i>k</i> < 14, -27 < <i>l</i> < 27	-17 < <i>h</i> < 20, -15 < <i>k</i> < 15, -27 < <i>l</i> < 17
measured reflections	7387	19141	23946	14912	22425	20540
independent reflections	2962 (<i>R</i> _{int} = 0.0372)	7783 (<i>R</i> _{int} = 0.0208)	8544 (<i>R</i> _{int} = 0.0339)	5355 (<i>R</i> _{int} = 0.0908)	9029 (<i>R</i> _{int} = 0.0199)	8466 (<i>R</i> _{int} = 0.0265)
completeness to θ	98.6	93.3	98.4	99.0	93.1	97.5
refinement method	full-matrix least-squares on <i>F</i> ²	full-matrix least-squares on <i>F</i> ²	full-matrix least-squares on <i>F</i> ²	full-matrix least-squares on <i>F</i> ²	full-matrix least-squares on <i>F</i> ²	full-matrix least-squares on <i>F</i> ²
data/restraints/parameters	2962/0/265	7783/4/565	8544/0/577	5355/0/541	9029/0/611	8466/0/645
goodness-of-fit on <i>F</i> ²	1.000	1.137	1.0036	1.149	1.023	1.055
final <i>R</i> indices [<i>I</i> > 2 ρ (<i>I</i>)]	<i>R</i> ₁ = 0.0314, <i>wR</i> ₂ = 0.0497	<i>R</i> ₁ = 0.0366, <i>wR</i> ₂ = 0.0843	<i>R</i> ₁ = 0.0342, <i>wR</i> ₂ = 0.0710	<i>R</i> ₁ = 0.0776, <i>wR</i> ₂ = 0.1715	<i>R</i> ₁ = 0.0322, <i>wR</i> ₂ = 0.0773	<i>R</i> ₁ = 0.0359, <i>wR</i> ₂ = 0.0916
<i>R</i> indices (all data)	<i>R</i> ₁ = 0.0575, <i>wR</i> ₂ = 0.0518	<i>R</i> ₁ = 0.0437, <i>wR</i> ₂ = 0.0867	<i>R</i> ₁ = 0.0502, <i>wR</i> ₂ = 0.0752	<i>R</i> ₁ = 0.1396, <i>wR</i> ₂ = 0.1899	<i>R</i> ₁ = 0.0458, <i>wR</i> ₂ = 0.0832	<i>R</i> ₁ = 0.0489, <i>wR</i> ₂ = 0.0968
largest diff. peak and hole [eÅ ⁻³]	0.165 and -0.185	0.985 and -0.542	0.739 and -0.713	2.101 and -0.771	0.929 and -0.586	1.116 and -0.531

^a Data taken from ref 18.

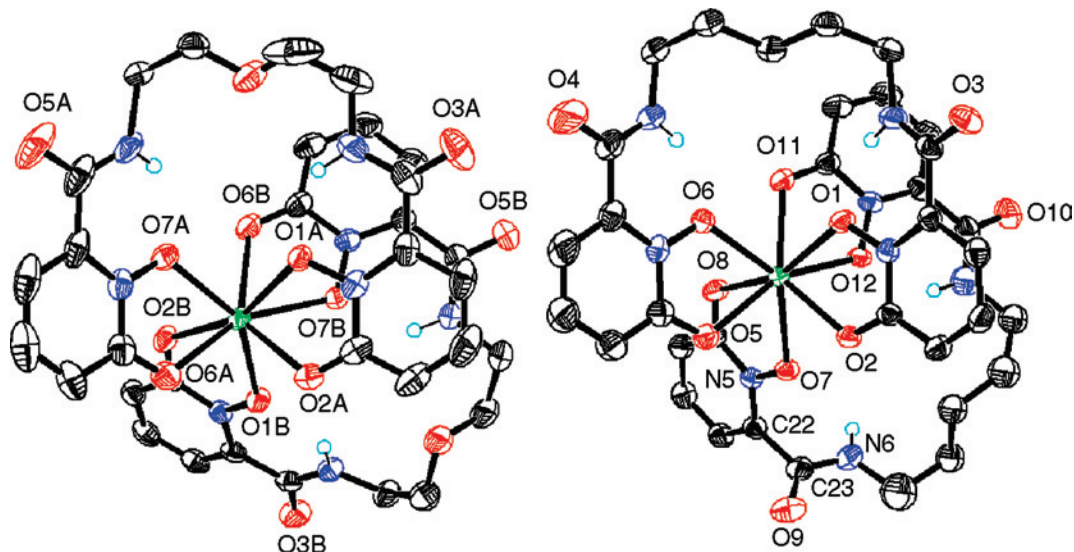


Figure 2. Comparison of reported¹⁸ crystal structures for $C_4H_{12}N^+[Eu(1)_2]^-$ (left) with the observed structure of $C_2H_8N^+[Eu(2)_2]^- \cdot (C_3H_7NO)_2$ (right). Only the major components of disordered ligand backbones are shown. The counteranions, cocrystallized solvent molecules, and selected H atoms have been omitted for clarity, and non-H atoms are drawn at the 50% probability level.

Table 2. Selected Bond Lengths for Ln(III) Complexes of 5LIO-1,2-HOPO (**H2I**) and 5LI-1,2-HOPO (**H22**)

$[Eu(1)_2]^-$	Eu–O1 (hydroxyl)	2.457	Eu–O2 (keto)	2.385	O1A–H2AB (amide)	1.926
	Eu–O7A(hydroxyl)	2.371	Eu–O6A (keto)	2.394	O1B–H2B1 (amide)	1.917
	Eu–O1B (hydroxyl)	2.372	Eu–O2B (keto)	2.383	O7A–H3AA (amide)	1.934
$[Eu(2)_2]^-$	Eu–O7B (hydroxyl)	2.434	Eu–O6B (keto)	2.380	O7B–H3BA (amide)	1.938
	Eu–O1 (hydroxyl)	2.400	Eu–O2 (keto)	2.387	O1–H4 (amide)	1.893
	Eu–O6 (hydroxyl)	2.373	Eu–O5 (keto)	2.413	O7–H22 (amide)	3.189
$[Sm(1)_2]^-$	Eu–O7 (hydroxyl)	2.422	Eu–O8 (keto)	2.382	O6–H15 (amide)	1.882
	Eu–O12 (hydroxyl)	2.375	Eu–O11 (keto)	2.380	O12–H41 (amide)	1.926
	Sm–O1A (hydroxyl)	2.429	Sm–O2A (keto)	2.423	O1–H104 (amide)	1.982
$[Sm(2)_2]^-$	Sm–O7A (hydroxyl)	2.368	Sm–O6A (keto)	2.427	O1B–H204 (amide)	1.917
	Sm–O1B (hydroxyl)	2.435	Sm–O2B (keto)	2.381	O7A–H113 (amide)	1.904
	Sm–O7B (hydroxyl)	2.394	Sm–O6B (keto)	2.421	O7B–H213 (amide)	2.011
$[Gd(1)_2]^-$	Sm–O1A (hydroxyl)	2.387	Sm–O2A (keto)	2.427	O1A–H104 (amide)	1.874
	Sm–O6A (hydroxyl)	2.405	Sm–O5A (keto)	2.398	O1B–H204 (amide)	3.253
	Sm–O1B (hydroxyl)	2.432	Sm–O2B (keto)	2.398	O6A–H115 (amide)	1.895
$[Gd(2)_2]^-$	Sm–O6B (hydroxyl)	2.383	Sm–O5B (keto)	2.396	O6B–H223 (amide)	1.926
	Gd–O1A (hydroxyl)	2.343	Gd–O2A (keto)	2.268	O1A–H4 (amide)	1.896
	Gd–O7A (hydroxyl)	2.332	Gd–O6A (keto)	2.331	O1B–H2 (amide)	1.961
	Gd–O1B (hydroxyl)	2.328	Gd–O2B (keto)	2.295	O7A–H5 (amide)	1.825
	Gd–O7B (hydroxyl)	2.327	Gd–O6B (keto)	2.318	O7B–H3 (amide)	1.875

(Ln = Eu, Sm, Gd) has been readily achieved using the appropriate 1:2 metal:ligand stoichiometry in the presence of pyridine acting as a base, and using MeOH as the solvent. After a short reflux period of ca. 4–6 h, the desired ML_2 complexes can be isolated upon cooling by filtration as the pyridinium salts in excellent yield and in analytically pure form. As detailed in the preceding communication,¹⁸ dissolving the isolated pyridinium salts of these complexes in an organic solvent such as MeOH or DMF in the presence of a smaller monocationic species such as tetramethylammonium or dimethylammonium followed by vapor diffusion with diethyl ether facilitated ready isolation of X-ray quality crystals, and we previously reported¹⁸ the structure of the $C_4H_{12}N^+[Eu(1)_2]^-$ complex. Herein, X-ray quality crystals were also obtained for the following complexes: $C_4H_{12}N^+[Sm(1)_2]^- \cdot CH_3OH \cdot H_2O$, $C_4H_{12}N^+[Gd(1)_2]^-$, $C_2H_8N^+[Eu(2)_2]^- \cdot (DMF)_2$, and $C_2H_8N^+[Sm(2)_2]^- \cdot (DMF)_{1.5}$ where $C_4H_{12}N^+$ and $C_2H_8N^+$ are the tetramethylammonium or dimethylammonium cations, respectively. For completeness, the crystal data for the previously reported and new complexes are both summarized in Table 1, and correspond-

ing views of these complexes are shown in Figures 2–4.

The $[Eu(2)_2]^-$ complex anion is shown in Figure 2, where the striking similarity to the previously reported $[Eu(1)_2]^-$ structure is also clearly evident. Relevant bond lengths are also summarized in Table 2. For both of these structures, the oxophilic Eu(III) cation is surrounded by a total of eight oxygen donors, four from each of the two bis-bidentate ligands, with average Eu–O bond lengths of ca. 2.40 Å. In both complexes, a commonly observed feature are the strong intramolecular hydrogen-bonding interactions between the amide proton and the adjacent coordinated *N*-hydroxyl oxygen atoms, with an average distance of 1.93 Å for $[Eu(1)_2]^-$ and 1.90 Å for $[Eu(2)_2]^-$. For the latter, only three of the four maximum possible interactions of this type were observed, as one of the amide groups in this complex lies twisted out of plane to the adjacent 1,2-HOPO ring systems (N6–C23–C22–N5 dihedral angle, $\theta = 84^\circ$). Significantly, this seemingly large distortion seems to have had little effect on the overall morphology of the final structure. For the $[Eu(1)_2]^-$ structure, the central ether oxygen of each ligand backbone is also involved in an intramolecular hydrogen-

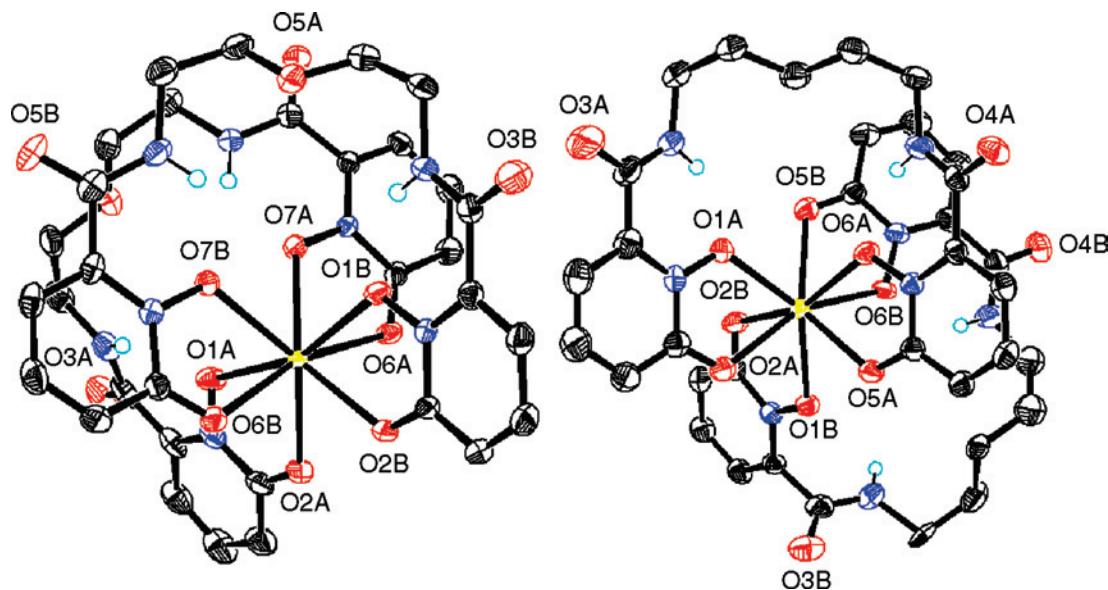


Figure 3. Comparison of observed structures for the $C_4H_{12}N^+[Sm(1)_2]^- \cdot CH_3OH \cdot H_2O$ (left) and $C_2H_8N^+[Sm(2)_2]^- \cdot (C_3H_7NO)_{1.5}$ (right) complexes. Only the major components of disordered ligand backbones are shown. The counteranions, cocrystallized solvent molecules, and selected H atoms have been omitted for clarity, and non-H atoms are drawn at the 50% probability level.

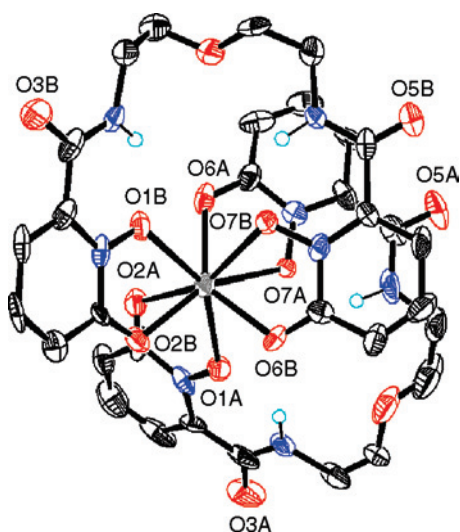


Figure 4. $C_4H_{12}N^+[Gd(1)_2]^-$ complex structure. The tetramethylammonium counteranion and selected H atoms have been omitted for clarity, and non-H atoms are drawn at the 50% probability level.

bonding interaction with the amide protons. Lastly, it is relevant to note that the orientation of each of the tetradentate ligands with respect to the other is almost identical between the two complexes, as shown in Figure 2.

The corresponding crystal structures for the ML_2 complexes of **H₂1** and **H₂2** with Sm(III) are shown in Figure 3, and relevant bond lengths are again summarized in Table 2. As was the case with Eu(III), each Sm(III) metal center is overall eight coordinate in each of the complex anions, with four donor atoms provided per ligand. The average Sm–O bond lengths are essentially identical, at ca. 2.41 Å, which are slightly larger when compared to the corresponding Eu(III) complexes (as expected due to the familiar lanthanide contraction⁴⁰). A closer analysis of Figure 3 reveals a major and very significant difference between the $[Sm(1)_2]^-$ and $[Sm(2)_2]^-$ structures. In the latter case, the orientation of each of the tetradentate ligands with respect to each other is

essentially identical to that observed for both Eu(III) complexes (see Figure 2) whereas for $[Sm(1)_2]^-$, the orientation of the two bis-bidentate ligands are quite different. Hence, for this complex, the two five atom linkages between each 1,2-HOPO chelate can be described as being located on the same “face” of the complex (forming a ca. -55° dihedral angle, as viewed down an imaginary rotational axis including the metal center and lying perpendicular to the page as drawn in Figure 3). By contrast, for the other three complexes discussed thus far, the five atom linker between each 1,2-HOPO chelate are offset by ca. 120° such that they lie almost on the opposite face of the complex. As evidenced by the similarity in coordinate bond lengths, however, this striking difference in orientation of the ligand backbones has little influence over the final structure of the complex. Nonetheless, it does serve to illustrate that each bis-bidentate chelate group is free to rotate with respect to the other, and it is likely the complexes will display fluxional behavior in solution.

Lastly, a view of the structure obtained for the $[Gd(1)_2]^-$ complex anion is shown in Figure 4, and relevant bond lengths are summarized in Table 2. Unfortunately, the quality of the crystal obtained for this complex was quite low, resulting in relatively poor diffraction data compared to the other complexes, but nonetheless, a tenable solution was obtained. In keeping with the expected lanthanide contraction, the smaller Gd(III) metal center exhibits slightly shorter Gd–O bond lengths, averaging 2.32 Å. The hydrogen-bonding pattern observed for the Eu(III) and Sm(III) complexes between amide N–H protons adjacent to the 1,2-HOPO ring system and the coordinated hydroxyl oxygen atom are maintained for the Gd(III) complex, as are the intramolecular H bonds to the central ether oxygen of the ligand. Lastly, the orientation of each ligand backbone with respect to the other again mimics that seen in both the Eu(III) complexes and also the structure of $[Sm(2)_2]^-$, where each

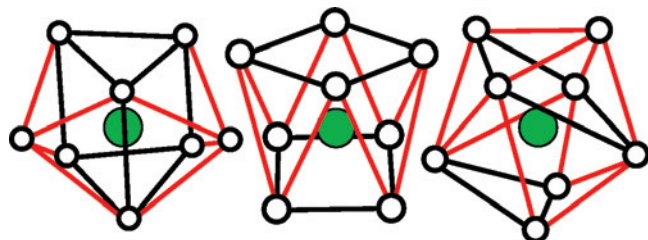


Figure 5. Three differing ideal coordination polyhedra of donor atoms (white spheres) for an eight coordinate Ln(III) metal center (green), from left to right, the bicapped trigonal prism (C_{2v}), the square antiprism (D_{4d}), and the trigonal dodecahedron (D_{2d}).

Table 3. Shape Measure Analyses of Ln(III) Complexes with 5LIO-1,2-HOPO (H_21) and 5LI-1,2-HOPO (H_22)

complex	square antiprism (D_{4d})	bicapped trigonal prism (C_{2v})	trigonal dodecahedron (D_{2d})
[Eu(1) $_2$] $^-$ ^a	22.82	23.01	28.42
[Eu(2) $_2$] $^-$	12.67	7.74	10.64
[Sm(1) $_2$] $^-$	14.47	11.06	9.67
[Sm(2) $_2$] $^-$	12.71	7.68	10.80
[Gd(1) $_2$] $^-$	6.90	10.57	14.98

^a Shape analysis results for [Eu(1)] $^-$ were erroneously reported in ref 18 to give C_{2v} as the closest match. The correct values are given here.

of the five atom linkages are on opposite faces of the structure, offset by a torsional angle of ca. 125°.

An important structural parameter which can also be obtained from the crystallographic data is the shape measure, SM,^{41,42} defined as:

$$SM = \min \left[\sqrt{\frac{1}{m} \sum_{i=1}^m (\delta_i - \theta_i)^2} \right]$$

This is a measure of the agreement in the variance of dihedral angles along all edges between the polyhedron derived from the crystal structure and the idealized cases. For the eight coordinate geometry, the three most common idealized coordination polyhedra are shown in Figure 5 and correspond to the bicapped trigonal prismatic (C_{2v}), square antiprismatic (D_{4d}), and trigonal dodecahedral (D_{2d}) geometries. The lowest value of SM for the three pairs represents the best fit to the closest idealized geometry, and resulting shape measure calculations for the five complexes studied herein are summarized in Table 3. It is readily apparent that the most common matches for the complexes were the bicapped trigonal prismatic (C_{2v}) or square antiprismatic (D_{4d}) geometries, while the [Sm(1) $_2$] $^-$ complex was trigonal dodecahedral (D_{2d}). Notably, it was for only this complex that the orientation of the five atom linkages between 1,2-HOPO chelate groups differed with respect to each other (vide supra), and this structural difference may also be partly responsible for the cause of the differing shape measure result.

Solution Thermodynamics. The protonation constants of 5LI-1,2-HOPO (H_22) were determined by potentiometry, with resulting parameters as summarized in Table 4. These values were also confirmed by spectrophotometric titrations and were subsequently used to determine the calculated molar

Table 4. Summary of pK_a Values and Eu(III) Binding Constants for Tetradentate 1,2-HOPO Ligands

	5LIO-1,2-HOPO (H_21) ^b	5LI-1,2-HOPO (H_22)
pK_{a1}	4.19(3)	4.52(3)
pK_{a2}	5.79(1)	5.65(1)
ΣpK_a	9.98	10.17
$pK_{a2} - pK_{a1}$	1.60	1.13
$\log_{10} \beta_{110}$	12.46(2)	12.33(1)
$\log_{10} \beta_{120}$	22.85(10)	22.56(5)
$\log_{10} \beta_{121}$	25.21(3)	25.40(1)
pEu^a	18.64(10)	18.35(5)

^a At pH = 7.4, [L] = 10 $^{-5}$ M, [Eu] = 10 $^{-6}$ M. ^b Data taken from ref 18.

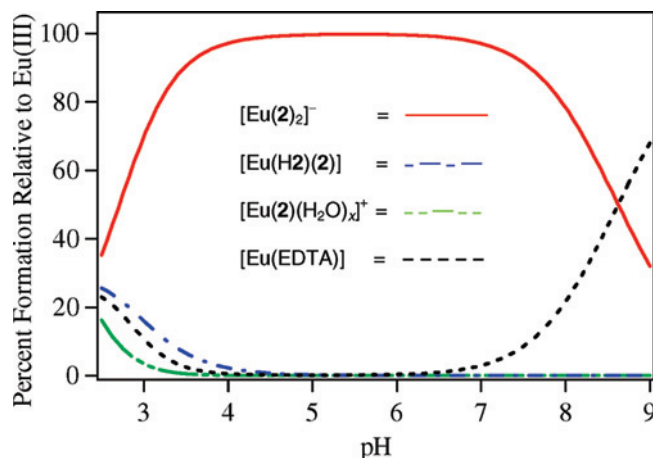


Figure 6. Speciation diagram for [Eu(2) $_2$] $^-$ under pM conditions (1 μ M Eu(III), 10 μ M ligand) in the presence of a 1000 fold excess of EDTA.

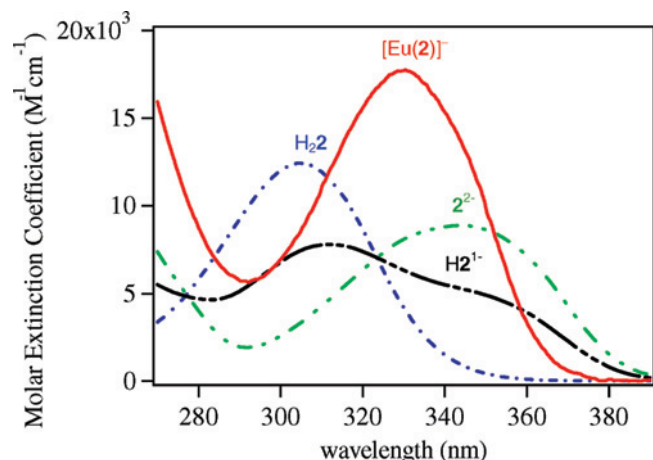


Figure 7. Calculated absorption spectra for the 5LI-1,2-HOPO ligand, H_22 (\cdots), its monoanion H_2^1- ($-\cdots-$), and dianion 2^{2-} ($---$). Corresponding spectra observed for the [Eu(2) $_2$] $^-$ complex in 0.1 M TRIS buffer at pH 7.4 are also shown.

absorbance of the neutral H_22 , anionic H_2^1- , and dianionic 2^{2-} forms of the ligand as shown in Figure 7. These can be compared directly to those previously reported¹⁸ for 5LIO-1,2-HOPO (H_21). As anticipated, the differing five carbon atom linkage has only a slight effect on the acidities of the two ligands.

It has been shown elsewhere⁴³ that the difference between pK_{a1} and pK_{a2} of a diprotic ligand can be used as a measure of the average separation between protonation sites. Applied to the current situation, the difference in pK_a values is slightly lower for H_22 at 1.13 compared to H_21 at 1.60 as shown in

(41) Porai-Koshits, M. A.; Aslanov, L. A. *Zhurnal Strukturnoi Khimii* **1972**, 13, 266–276.

(42) Kepert, D. L. *Prog. Inorg. Chem.* **1978**, 24, 179–249.

(43) Adams, E. Q. *J. Am. Chem. Soc.* **1916**, 38, 1503–1510.

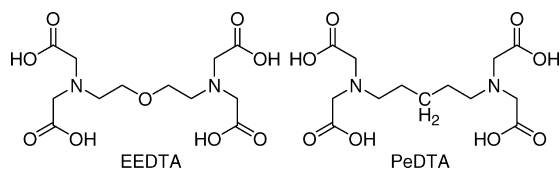
Chart 2. Structural Analogues of the Ligand Scaffolds for the 1,2-HOPO Ligands

Table 4. Since both the 5LI- and 5LIO- backbones span approximately the same distance when fully elongated, it is reasonable that the differing protonation behavior as expressed by the difference in pK_a values can be attributed to the presence of the central ether oxygen atom of the latter, resulting in a closer intermolecular distance on average between protonation sites. This can be rationalized by the presence of an intervening hydrogen-bonding network, as drawn in Chart 1, involving the amide protons and the central ether oxygen, which ensures that the two *N*-hydroxamate functional groups remain in close proximity and may also preorganize the 5LIO-1,2-HOPO ligand for metal chelation. The presence of this hydrogen-bonding network for 5LIO-1,2-HOPO may also account for the slight difference in pK_a values observed between the two differing ligands.

From the sum of pK_a values (equivalent to the overall ligand acidity), it can be anticipated that H_22 , as the more basic ligand, will form a more stable ML_2 complex than H_21 . Unfortunately, the cumulative formation constants with Eu(III) could not be measured directly, since Eu(III) was not released at pH values as low as 1.6 under the experimental conditions utilized. Hence, competition titration experiments as described elsewhere¹⁸ using DTPA as a known competitor were required to experimentally determine β_{120} , and this number was then fixed in subsequent refinements of potentiometric low pH titration data to obtain β_{110} and β_{121} , with the resulting parameters as summarized in Table 4. While the β_{120} (and pEu values) are quite similar, a close inspection of this data reveals the expected improvement in ML_2 complex stability for the H_22 ligand was not borne out experimentally, instead revealing the H_21 ligand forms the more stable ML_2 chelate, with pEu = 18.65 (10) for $[Eu(1)_2]^-$ versus pEu = 18.35 (5) for $[Eu(2)_2]^-$. As a rationale for this apparent inconsistency in chelate strengths, again, a consideration of the hydrogen-bonding network operant between the two 1,2-HOPO units, and hence the rigidity of the backbone, is instructive.

In the present case, hydrogen-bonding interactions between the amide protons and the ether oxygen were observed crystallographically and it can be assumed that these hydrogen-bond interactions will persist in solution. The effect of these interactions would be to rigidify the ligand and hence confer a slightly improved chelate effect, therefore increasing the stability for the ensuing H_21 based complexes. For the aminocarboxylate ligands EEDTA and PeDTA (Chart 2), conditional stability measurements yielded pM values of 15.73 and 8.07, respectively, with Gd(III).^{35,44} In this case,

it was presumed that the ether oxygen atom of EEDTA is also coordinated to the metal ion, which would contribute ca. 1.6 log units per oxygen atom coordinated. The remaining difference in stability of ca. 4 log units was attributed to the effect of rigidifying the scaffold. In the present case, the less pronounced difference observed in Eu(III) complex stability between H_21 or H_22 is most likely due to a less optimal geometry for these intramolecular hydrogen-bonding interactions.

Lastly, as further evidence of the $[Eu(1)_2]^-$ and $[Eu(2)_2]^-$ complex stabilities, a comparison with ethylenediaminetetraacetic acid (EDTA) can be made. EDTA is a common assay component used in biological samples (usually for the removal of Fe(III) or other interfering metal cations) which also forms relatively strong octadentate complexes with the oxophilic Ln(III) cation (e.g. pEu = 15.48). It is worthy then to note that, under pM conditions, the present $[Eu(1)_2]^-$ or $[Eu(2)_2]^-$ complexes can tolerate as much as a 1000 fold excess of EDTA relative to Eu(III), even though they are only tetradentate ligands, with no significant impact on the speciation and consequent luminescence intensity (<7% decrease) as demonstrated in Figure 6.

Photophysics. The absorption spectra of the ligand H_22 in its various protonation states are shown in Figure 7, together with that of the $[Eu(2)_2]^-$ complex. Notably, the absorption spectrum of H_22 is essentially identical to that reported previously for H_21 .¹⁸ Specifically, either ligand with the 5LI- or 5LIO- backbones yields a broad electronic envelope in the near UV assigned to a transition with mixed $n \rightarrow \pi^*$, $\pi \rightarrow \pi^*$ parentage (vide infra) with an apparent maxima at ca. 305 nm ($\epsilon \sim 12\,400\text{ M}^{-1}\cdot\text{cm}^{-1}$). Upon deprotonation of either ligand to form the dianionic species, this band shifts to ca. 345 nm and is reduced slightly in intensity ($\epsilon \sim 8\,900\text{ M}^{-1}\cdot\text{cm}^{-1}$).

Corresponding electronic structure calculations using TD-DFT were also performed using Gaussian'03⁴⁵ in order to further characterize the excited-state of the 1,2-HOPO chromophore. As a simplified model, only the 6-methyl amide of 1,2-HOPO was used as the input structure, and this was first geometry optimized with no symmetry constraints to give the relaxed output geometry shown in Figure 8. The output geometry obtained is reasonable, with all non-H atoms lying essentially in a single plane. The calculated structure also reproduced the expected strong H-bonding interactions between the *N*-hydroxyl proton and adjacent keto

(44) Bianchi, A.; Calabi, L.; Corana, F.; Fontana, S.; Losi, P.; Maiocchi, A.; Paleari, L.; Valtancoli, B. *Coord. Chem. Rev.* **2000**, *204*, 309–393.

(45) Frisch, M. J.; Trucks, G. W.; Schlegel, H. B.; Scuseria, G. E.; Robb, M. A.; Cheeseman, J. R.; Montgomery, J. A., Jr.; Vreven, T.; Kudin, K. N.; Burant, J. C.; Millam, J. M.; Iyengar, S. S.; Tomasi, J.; Barone, V.; Mennucci, B.; Cossi, M.; Scalmani, G.; Rega, N.; Petersson, G. A.; Nakatsuji, H.; Hada, M.; Ehara, M.; Toyota, K.; Fukuda, R.; Hasegawa, J.; Ishida, M.; Nakajima, T.; Honda, Y.; Kitao, O.; Nakai, H.; Klene, M.; Li, X.; Knox, J. E.; Hratchian, H. P.; Cross, J. B.; Bakken, V.; Adamo, C.; Jaramillo, J.; Gomperts, R.; Stratmann, R. E.; Yazyev, O.; Austin, A. J.; Cammi, R.; Pomelli, C.; Ochterski, J. W.; Ayala, P. Y.; Morokuma, K.; Voth, G. A.; Salvador, P.; Dannenberg, J. J.; Zakrzewski, V. G.; Dapprich, S.; Daniels, A. D.; Strain, M. C.; Farkas, O.; Malick, D. K.; Rabuck, A. D.; Raghavachari, K.; Foresman, J. B.; Ortiz, J. V.; Cui, Q.; Baboul, A. G.; Clifford, S.; Cioslowski, J.; Stefanov, B. B.; Liu, G.; Liashenko, A.; Piskorz, P.; Komaromi, I.; Martin, R. L.; Fox, D. J.; Keith, T.; Al-Laham, M. A.; Peng, C. Y.; Nanayakkara, A.; Challacombe, M.; Gill, P. M. W.; Johnson, B.; Chen, W.; Wong, M. W.; Gonzalez, C.; Pople, J. A. *Gaussian 03*, revision C.02; Gaussian, Inc.: Wallingford, CT, 2004.

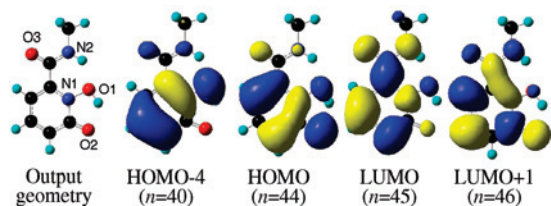


Figure 8. Calculated output geometry obtained from static B3LYP/6-311G++ (d,p) geometry optimization and corresponding molecular orbital diagrams from TD-DFT electronic structure calculations for a model 6-MeAmide-1,2-HOPO chromophore. Isodensity = 0.02.

oxygen (O1–H···O2 = 1.79 Å) and, similarly, between the amide proton and the *N*-hydroxyl oxygen atom (N2–H···O1 = 1.89 Å).

A summary of the electronic structure calculation is given in Table 5 and consideration of these results revealed the nature of the first excited singlet state of the 1,2-HOPO chromophore can be described principally by a HOMO → LUMO excitation, with a smaller contribution from the HOMO – 4 → LUMO + 1 excitation. Inspection of the relevant Kohn–Sham molecular orbitals also shown in Figure 8 reveal these transitions to be mixed π – π^* and n – π^* , respectively. Similarly, the nature of the lowest triplet state (T_0) can be described principally by a HOMO → LUMO excitation, i.e. a ${}^3\pi\pi^*$ transition.

The absorption spectrum of $[\text{Eu}(\mathbf{2})_2]^-$ is also shown in Figure 7 and is again almost identical to that previously observed¹⁸ for $[\text{Eu}(\mathbf{1})_2]^-$ (Table 6). Specifically, the ML₂ complexes for either (**1**) or (**2**) with both Eu(III) or Sm(III) gave essentially identical absorption profiles, with an apparent maximum at ca. 330 nm ($\epsilon_{\text{max}} = 9200 \text{ M}^{-1}\cdot\text{cm}^{-1}$) assigned to a transition with mixed $n \rightarrow \pi^*$ and $\pi \rightarrow \pi^*$ parentage.

A second TD-DFT calculation was also performed using Gaussian'03⁴⁵ in order to further characterize the excited-state of the anionic 1,2-HOPO chromophore in complex with a metal cation. However, rather than performing computationally expensive calculations involving a trivalent lanthanide, we have adopted an approach analogous to that reported⁴⁶ previously by Picard et al., in this case, replacing the *N*-hydroxyl proton with a monovalent Na⁺ cation and adopting a bidentate chelating mode for the oxygen atoms in order to mirror the binding mode of a trivalent Ln(III) cation. While this is undoubtedly a crude model, we have found this approach to be quite useful as a tool for understanding the electronic structure. It must also be stressed that the goal of this “calculation” is not to determine the electronic states of the Ln(III) cation but rather to approximate the energy for the lowest excited singlet and triplet states of the ligand.

The resulting output geometry shown in Figure 9 where it is evident that all non-H atoms are essentially lying in a plane and also that the Na⁺ cation has retained its bidentate coordination mode upon energy minimization. Bond lengths obtained between the sodium and O1 and O2 were 2.16 and 2.14 Å, respectively, slightly smaller than those observed

with Eu(III) by X-ray crystallography. Nonetheless, the geometries are very similar and a common feature of both the Na⁺ model and the Eu(III) X-ray structures is the conserved intramolecular H-bonding interaction between the amide proton and *N*-hydroxyl oxygen atom.

The resulting electronic structure calculation is again summarized in Table 5, and relevant Kohn–Sham molecular orbitals are shown in Figure 9. Hence, the nature of the lowest energy triplet excited-state for the Na⁺ complex of an anionic 1,2-HOPO chromophore can be described principally by a HOMO → LUMO + 1 excitation with ${}^3\pi\pi^*$ character, as was the case for the free ligand. Significantly, an inspection of the orbitals involved in the lowest energy singlet transition (from HOMO → LUMO) demonstrates obvious ¹LMCT (ligand to metal charge transfer) character. However, the ca. 3.2 eV energy calculated for this transition did not match any experimentally observed absorption at ca. 380 nm, for either of the ligands **1** or **2** deprotonated with NaOH, or indeed the absorption spectrum observed for the Eu(III) complexes. It has been noted⁴⁷ that TD-DFT calculations using simple exchange correlational (xc) functionals such as the B3LYP/6-311G++ (d,p) basis set used here can yield substantial errors when estimating the excitation energy of charge transfer (CT) type transitions, due to self-interaction errors within the orbital energies of the ground-state DFT calculation. We conclude that it is likely this calculated transition is an artifact, and the ¹LMCT likely lies at much higher energy. A corresponding configuration interaction singles (CIS) calculation which is not subject to the same self-interaction error was also performed using the identical input geometry, and the resulting value estimated for the same HOMO–LUMO transition was located at significantly higher energy (ca. 4.89 eV, 253.4 nm). For the local valence excited states, the results from TD-DFT will be more reliable. Indeed, the estimated $S_0 \rightarrow S_2$ transition calculated using this technique at 3.755 eV can be described principally by a HOMO → LUMO + 1 excitation, for which both Kohn–Sham orbitals are ligand centered (LC), and this transition can be readily assigned $\pi \rightarrow \pi^*$ character. The calculated position of this absorption at ca. 330 nm is in excellent agreement with those observed for both the Eu(III) and Sm(III) complexes of **1** and **2**.

The normalized emission spectra for the $[\text{Eu}(\mathbf{2})_2]^-$ and $[\text{Sm}(\mathbf{2})_2]^-$ complexes are shown in Figure 10, and relevant photophysical data are summarized in Table 6. The emission spectrum of the Eu(III) complex is characteristic of the metal, with well-resolved transitions from the metal centered ⁵D₀ excited-state to ⁷F_{*J*} ground-state multiplet readily apparent. Maximum intensities at 593, 612, 652, and 702 nm, respectively, were observed for the *J* = 1, 2, 3, and 4 transitions and, as was the case for the $[\text{Eu}(\mathbf{1})_2]^-$ complex, the *J* = 2 so-called “hypersensitive” transition is extremely intense for both the pure alkyl and alkyl–ether linked backbones. The resulting luminescence quantum yields for the $[\text{Eu}(\mathbf{2})_2]^-$ complex in 0.1 M TRIS buffer at pH 7.4 were determined (relative to quinine sulfate in 1.0 N H₂SO₄, $\Phi_{\text{ref}} = 0.546$) and are comparable with

(46) Gutierrez, F.; Tedeschi, C.; Maron, L.; Daudey, J.-P.; Azema, J.; Tisnes, P.; Picard, C.; Poteau, R. *THEOCHEM* **2005**, *756*, 151–162.

(47) Dreuw, A.; Head-Gordon, M. *J. Am. Chem. Soc.* **2004**, *126*, 4007–4016.

Table 5. Summary of Electronic Structure Calculations for 1,2-HOPO Chromophore and Na⁺ Complex

excited state	multiplicity	energy (eV)	wavelength (nm)	oscillator strength	orbital(s) involved ($n \rightarrow n'$)	transition coefficient
6-MeAmide-1,2-HOPO						
1	T ₀	2.542	487.72	0.0000	44 → 45	0.7764
2	T ₁	3.529	351.37	0.0000	43 → 45 43 → 46 43 → 52	0.7083 -0.1733 -0.2036
3	T ₂	3.706	334.55	0.0000	41 → 45 42 → 45 42 → 46 42 → 52	0.1085 0.6903 -0.1149 -0.1241
4	T ₃	3.708	334.38	0.0000	40 → 45 44 → 46 44 → 52	0.4211 0.6292 -0.1300
5	S ₁	3.8185	324.69	0.1395	40 → 46 44 → 45	-0.1235 0.6385
[Na(6-MeAmide-1,2-HOPO)]						
1	T ₀	2.649	468.05	0.0000	49 → 51	0.7643
2	T ₁	3.186	389.15	0.0000	49 → 50	0.7035
3	S ₁	3.205	386.85	0.0060	49 → 50	0.7039
4	T ₂	3.2404	382.62	0.0000	47 → 51 48 → 51	0.2295 0.6406
					49 → 53 49 → 55	-0.1884 0.3529
5	S ₂	3.755	330.18	0.1066	48 → 55 49 → 51	-0.1331 0.6356

Table 6. Summary of Photophysical Data for Complexes of Tetradentate 1,2-HOPO Ligands^a

complex	λ_{\max} (nm)	ϵ (M ⁻¹ ·cm ⁻¹)	Φ_{tot} (%)	τ (μ s)	k_r (calcd) ^c (ms ⁻¹)	k_{nr} (calcd) ^c (ms ⁻¹)
[Eu(5LIO-1,2-HOPO) ₂] ^{-*}	332.7	19,250	21.5	727 (1012) ^b	0.61	0.81
[Eu(5LI-1,2-HOPO) ₂] ⁻	331.4	18,800	20.7	737 (996.2) ^b	0.62	0.74
[Sm(5LIO-1,2-HOPO) ₂] ⁻	333.0	19,200	0.44	13.4	N/A	N/A
[Sm(5LI-1,2-HOPO) ₂] ⁻	331.3	19,400	0.44	10.7	N/A	N/A

^a Data taken from ref 18. ^b Corresponding value obtained with D₂O as solvent. ^c Calculated from the ratio of the integrated area for the $J = 1$ transition compared to the total integrated area as per the method described in ref 48.

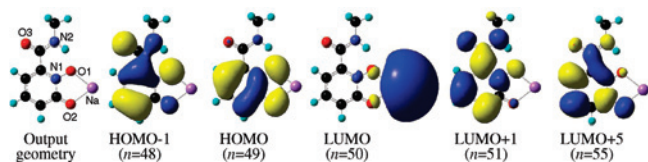


Figure 9. Calculated output geometry obtained from static B3LYP/6-311G++ (d,p) geometry optimization and corresponding molecular orbital diagrams from TD-DFT electronic structure calculations for a model [Na(6-MeAmide-1,2-HOPO)] complex. The metal centered character of the LUMO is an artifact of the B3LYP functional calculation (see text). Isodensity = 0.02.

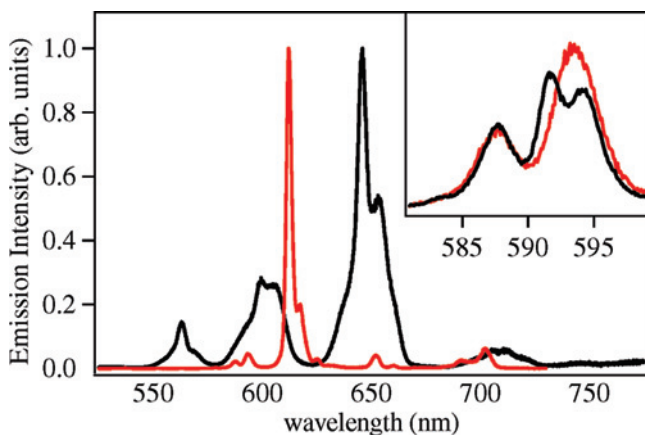


Figure 10. Normalized emission spectra ($\lambda_{\text{ex}} = 330$ nm) for 1×10^{-6} M solutions of the Eu(III) (red) and Sm(III) (black) ML₂ complexes of (2) in 0.1 M TRIS buffer at pH 7.4 ($\lambda_{\text{ex}} = 330$ nm). (inset) Comparison of solid state (black) and solution (red) emission spectra for the [Eu(2)₂]⁻ complex in the ⁵D₀ → ⁷F₁ spectral region.

those obtained¹⁸ for [Eu(1)₂]⁻. Evidently, slight structural modification of the tetradentate ligand involving replacement of the ether oxygen in the latter with a methylene group in [Eu(2)₂]⁻ has little influence over the resulting photophysical behavior, with resulting Φ_{tot} values essentially identical within experimental error. This is further corroborated by the similarity in radiative (k_r) and nonradiative (k_{nr}) decay rate constants calculated using the method of Werts et al.⁴⁸ by comparing the

integrated intensities of the $J = 1$ transition to the total integrated area of the corrected emission spectrum (Table 6).

Corresponding time-resolved photophysical decay parameters for both complexes are also summarized in Table 6, using both H₂O and D₂O as solvent, which allowed the hydration number, “ q ” to be determined, according to a recently reported⁴⁹ improvement of the Horrock’s equation:

$$q = A' (k_H - k_D - B)$$

where A' and B are empirical constants of 1.11 and 0.31 ms⁻¹ for Eu(III) and k_D and k_H represent the observed luminescence decay rate constants, k_{obs} , in deuterated and nondeuterated solvent, respectively. The resulting values for q were both essentially zero (0.09 ± 0.1 [Eu(1)₂]⁻ and 0.05 ± 0.1 [Eu(2)₂]⁻) in accordance with the anticipated eight-coordinate geometry and in agreement with the Eu(III) structures observed by crystallography.

Given the availability of crystalline X-ray quality samples for [Eu(1)₂]⁻ and [Eu(2)₂]⁻, we were also able to perform solid state luminescence studies of the complexes, for which the coordination geometry is well-characterized. First, the metal centered luminescence lifetimes obtained for both [Eu(1)₂]⁻ and [Eu(2)₂]⁻ were consistently shorter than the corresponding solution measurements (ca. 630 μ s cf. 730 μ s in H₂O), which may be attributed to a self-quenching mechanism operant in the closely packed solid (Eu•••Eu ~ ca. 9 Å) as seen elsewhere for other Ln(III) systems.⁵⁰ Of considerable more interest, however, was a closer inspection of the solid state compared with solution spectra in the region of the ⁵D₀ → ⁷F_{0,1} and ⁵D₀ → ⁷F₂ transitions from 575 to

(48) Werts, M. H. V.; Jukes, R. T. F.; Verhoeven, J. W. *Phys. Chem. Chem. Phys.* **2002**, *4*, 1542–1548.

(49) Supkowski, R. M.; Horrocks, W. D., Jr *Inorg. Chim. Acta* **2002**, *340*, 44–48.

(50) Muller, G.; Schmidt, B.; Jiricek, J.; Hopfgartner, G.; Riehl, J. P.; Bünzli, J.-C. G.; Piguet, C. *J. Chem. Soc., Dalton Trans.* **2001**, 2655–2662.

Table 7. Analysis of Crystal Field Splitting under Various Site Symmetries for the Most Common Eight-Coordinate Ln(III) Geometries and Separation into Corresponding Symmetry Allowed Electronic Transitions^a

CN = 8	site symmetry	⁵ D ₀ → ⁷ F ₀ (ED)	⁵ D ₀ → ⁷ F ₁ (MD)	⁵ D ₀ → ⁷ F ₂ (ED)
bicapped trigonal prism	C _{2v}	A ₁	A ₂ , B ₁ , B ₂	2A ₁ , B ₁ , B ₂
square antiprism	D _{4d}	none	A ₂ , E ₃	E ₁
trigonal dodecahedron	D _{2d}	none	A ₂ , E	B ₂ , E

^a ED and MD in parenthesis indicate the principal character and hence selection rules used for each transition, which are either induced electrical dipole or magnetic dipole, respectively.

600 nm and 600 to 640 nm respectively.

Importantly, for both complexes, a single ⁵D₀ → ⁷F₀ transition is observed, indicative of a single emitting species present in solution and enabling site symmetry determination.⁵¹ For the ⁵D₀ → ⁷F₁ transition, crystal field splitting of the *J* = 1 level results in a maximum of three (2*J* + 1) peaks in a low symmetry environment (e.g. C_{2v}) versus only two peaks for the hexagonal, trigonal, or tetragonal point groups (e.g. D_{2d}, D_{4d}). The expected transitions derived from their principal character (either magnetic or electrical dipole) are shown in Table 7 for the three most common eight-coordinate Ln(III) geometries that were shown previously in Figure 5.

As shown in the inset of Figure 10, three peaks are clearly evident in the ⁵D₀ → ⁷F₁ region of the luminescence spectrum for a microcrystalline sample of [Eu(2)₂]⁻, with maxima at 587.7, 591.6, and 594.1 nm. While the limited resolution (ca. 0.3 nm) of the fluorescence spectrometer precludes a definitive determination of the exact point group of the complex, the data in Table 7 show that for the three most common coordination polyhedra, the best match to the observed luminescence spectra is obtained for the bicapped trigonal prism (C_{2v}) geometry. It is certainly notable that this result agrees with the structure from X-ray crystallography, which shape analysis showed to be closest to C_{2v} geometry.

By contrast, the corresponding emission spectrum from aqueous solution of [Eu(2)₂]⁻ gave only two discernible peaks at 587.7 and 593.5 nm, behavior indicative of a solution structure with higher symmetry than that observed in the solid state. Again, the data in Table 7 imply D_{4d} or D_{2d} symmetries, and further analysis of the band shape for the *J* = 2 band at ca. 610 nm shows a distinct splitting of this band into two components (a smaller shoulder evident to lower energy), suggesting D_{2d} symmetry as the closest match between the three idealized coordination polyhedra. Returning to the results from shape analysis for the [Sm(1)₂]⁻ complex, it was noted that this complex had the closest match to D_{2d} site symmetry, and in this case, the ligand scaffolds were located on the same face of the complex. As such, we may tentatively correlate this change in symmetry upon dissolution to the presence of an ensemble of emitting species, most with predominantly D_{2d} symmetry. This differing symmetry when compared to the solid state structure can be realized in solution by free rotation of one ligand with respect to the other (about the central metal ion), although, given the millisecond lifetime of the Eu(III)

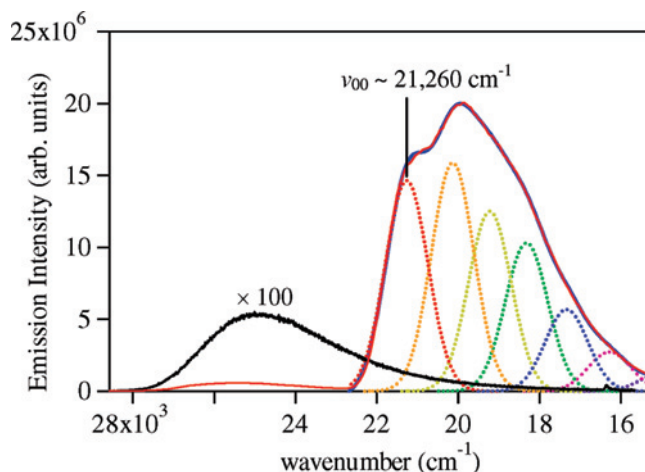


Figure 11. Comparison of room temperature (×100, black) and 77 K (red) emission spectra of the [Gd(1)]⁻ complex, with spectral deconvolution (blue) of the latter into a vibronic progression of several overlapping Gaussian functions with separations of ca. 1000–1100 cm⁻¹ to determine *v*₀₀ of the T₀ energy.

luminescence, it is not possible to determine whether this change in symmetry occurs prior to or subsequent to formation of the excited state.

Metal centered luminescence was also seen as a faint pink emission upon UV irradiation from the Sm(III) complexes of **1** and **2**, with several apparent maxima evident at ca. 563, 599, 646, and 710 nm corresponding to transitions from the ⁴G_{5/2} excited-state to lower ⁶F_{*J*} and ⁶H_{*J*} levels. As shown in Figure 10, the most intense of these was the ⁴F_{9/2} → ⁶H_{9/2} apparent at ca. 646 nm. As was the case for the Eu(III) complexes, the spectra of either complex with **1** or **2** are essentially identical and the corresponding luminescence quantum yields and lifetimes are also summarized in Table 6. Notably, the Sm(III) spectra are less amenable to structural interpretation due to increased degeneracy of the states involved compared with Eu(III), and hence, the corresponding solid state experiments were not performed.

The potential for ML₂ complexes of **1** and **2** to sensitize other visible emitting lanthanide cations, notably Dy(III) and Tb(III), was also evaluated; however, metal centered luminescence was only noted for the Eu(III) and Sm(III) complexes. This behavior can be rationalized by a comparison and analysis of the room temperature and low temperature (77 K) phosphorescence spectra for the [Gd(1)₂]⁻ complex (which lacks a low energy metal centered acceptor level) in a 1:1 EtOH:MeOH (v/v) glassing solvent, shown in Figure 11. At room temperature, relative ligand centered emission from the Gd(III) complex is very weak, with a faint signal attributed to singlet emission from the ligand apparent at ca. 400 nm. However, upon cooling to 77 K, this singlet emission is enhanced and a much more intense band appears from 450 to 600 nm, which can be attributed to phosphorescence from the ligand T₀ state. While this band displayed a poorly resolved vibronic progression, the *v*₀₀ electronic origin could not be unambiguously assigned. Rather, the lowest T₀ energy was estimated by spectral deconvolution of the 77 K luminescence signal into several overlapping

(51) Bünzli, J.-C. G.; Choppin, G. R. *Lanthanide Probes in Life, Chemical and Earth Sciences: Theory and Practice*; 1989.

Gaussian functions to approximate an unresolved vibrational progression of ca. 1000–1100 cm^{-1} . The resulting T_0 energy was evaluated to be ca. 21,260 cm^{-1} , which is remarkably similar to the value estimated using TD-DFT methods for the [Na(6-MeAmide-1,2-HOPO)] complex of 21 365 cm^{-1} .

From the experimentally observed triplet energy, the sensitizing properties of the 1,2-HOPO chromophore can be readily understood in terms of the so-called energy gap law,^{52,53} since the energy of this level is located ca. 2230 and 3980 cm^{-1} higher in energy than the potential 5D_1 and 5D_0 accepting levels in Eu(III), which facilitates efficient energy transfer. Similarly, for Sm(III), the T_0 energy of the ligand is ca. 3360, 2360, and 1210 cm^{-1} higher than the corresponding $^4G_{5/2}$, $^4F_{3/2}$, and $^4G_{7/2}$ levels. By contrast, the lowest energy Tb(III) and Dy(III) acceptor levels are at 20 400 (5D_4) and 21 100 cm^{-1} ($^4F_{9/2}$), both of which are only slightly lower in energy than the T_0 state, and much less than the ca. 2500 cm^{-1} energy gap necessary to promote efficient sensitization of these metal centers.^{52,53}

Conclusions

The 1-hydroxy-2-pyridinone chelate group has proven to be a remarkably efficient sensitizer for Eu(III), which also forms extremely stable complexes in aqueous solution. The resistance to decomplexation of compounds of the type described herein, despite the presence of strong competitors such as EDTA, will be essential for their practical usage in bioanalytical applications. Furthermore, this chelate group can now be readily accessed, and the synthetic intermediates outlined herein allow for ease of systematic variations in the

backbone connecting bis-bidentate ligands and also allow for the preparation of more complex hexa- and octadentate derivatives.

A thorough investigation of the photophysical properties for these Eu(III) 1,2-HOPO complexes, including the location of the lowest energy triplet state, prompted our investigation with Sm(III) and has elucidated a more complete understanding of the sensitization process in terms of the energy gap between the excited singlet and triplet levels. Similarly, the results gained from TD-DFT calculations were advantageous in deciphering the electronic structure and agreed well with the experimental data, despite the obvious simplicity of the model. Indeed, these results may prove useful as a predictive tool to guide synthetic efforts, at least in as far as ligand centered transitions can be predicted with a high level of accuracy.

Acknowledgment. This work was partially supported by the NIH (Grant HL69832) and supported by the Director, Office of Science, Office of Basic Energy Sciences, and the Division of Chemical Sciences, Geosciences, and Biosciences of the U.S. Department of Energy at LBNL under Contract No. DE-AC02-05CH11231. This technology is licensed to Lumiphore, Inc. in which some of the authors have a financial interest. Financial support was provided to C.J.J. by the German Research Foundation (DFG). The authors thank Dr. Kathleen Durkin and Ms. Amanda Samuel for assistance with the TD-DFT calculations and Mr. Gēza Szigethy for assistance with the shape analysis calculations.

Supporting Information Available: X-ray crystallographic files (in CIF format) and Gaussian'03 output from TD-DFT and CIS calculations (in ASCII format). This material is available free of charge via the Internet at <http://pubs.acs.org>.

IC702144N

(52) Latva, M.; Takalo, H.; Mukkala, V.-M.; Matachescu, C.; Rodriguez-Ubis, J. C.; Kankare, J. *J. Lumin.* **1997**, *75*, 149–169.

(53) Arnaud, N.; Georges, J. *Spectrochim. Acta A, Mol. Biomol. Spectrosc.* **2003**, *59*, 1829–1840.